Numerical Heat Transfer

PC SOLUTIONS FOR HEAT TRANSFER AND FLUID FLOW DOWNSTREAM OF AN ABRUPT, ASYMMETRIC ENLARGEMENT IN A CHANNEL

E. M. Sparrow [a] & W. Chuck [a]

[a] Department of Mechanical Engineering , University of Minnesota , Minneapolis, Minnesota, 55455
Published online: 27 Feb 2007.

PLEASE SCROLL DOWN FOR ARTICLE

PC SOLUTIONS FOR HEAT TRANSFER AND FLUID FLOW DOWNSTREAM OF AN ABRUPT, ASYMMETRIC ENLARGEMENT IN A CHANNEL

E. M. Sparrow and W. Chuck

Department of Mechanical Engineering, University of Minnesota, Minneapolis, Minnesota 55455

An IBM PC was used to obtain finite-difference solutions to a complex heat transfer and fluid flow problem in which the solution domain contained nearly 6000 grid points. The investigated problem was the abrupt, asymmetric enlargement of a parallel-plate channel. The enlargement takes the form of a backward-facing step, the presence of which causes separation of the flow. Heat transfer occurred at the channel wall which extended downstream from the foot of the step. The present velocity solutions were shown to be at least as accurate as prior numerical solutions and served to extend the range of investigated enlargements. The variation of the local Nusselt number with the Reynolds number took on different forms at various axial distances from the enlargement step. In a region extending downstream from the step, the Nusselt number actually decreased monotonically with increasing Reynolds number. Farther downstream, the Nusselt-Reynolds variation was monotonically increasing, while still farther downstream, the Nusselt number was independent of the Reynolds number.

INTRODUCTION

This paper conveys a description of the methodology and the results for finite-difference solutions of laminar fluid flow and heat transfer downstream of an abrupt, asymmetric enlargement in a parallel-plate channel. The numerical work was performed on an IBM PC utilizing nearly 6000 grid points, thereby demonstrating the capabilities of personal computers in solving complex problems of convective heat transfer. In addition to highlighting the potential of the PC, heretofore unavailable heat transfer results were obtained, and the available velocity field results were extended to a wider range of the channel enlargement ratio. The relevant literature will be surveyed shortly.

A schematic diagram of the physical problem to be investigated is presented in Fig. 1. The diagram shows a side view of the portion of the channel adjacent to the enlargement. Fluid is delivered to the enlargement by an adiabatic-walled channel of height h_{in} which is long enough to provide fully developed flow at the enlargement cross section. It should be noted, however, that at sufficiently low Reynolds numbers, a precursive effect of the enlargement is felt upstream of the enlargement cross section, causing departures from the developed velocity distribution.

Downstream of the enlargement, the channel is of height h and is of sufficient length so that exit effects, if any, do not affect the flow and heat transfer in the region to be investigated here. In the enlarged channel, the lower wall is at a uniform

NOMENCLATURE

H	dimensionless height of enlarged channel $(=h/z)$	V	dimensionless transverse velocity $(=v/\bar{u}_{in})$
h	height of enlarged channel	v	transverse velocity
h_{in}	height of pre-enlargement channel	X	dimensionless axial coordinate $(=x/z)$
k	thermal conductivity		
LMTD	log-mean temperature difference	X_{mn}	difference between X_m and X_n
Nu_x	local Nusselt number [Eq. (38)]	x	axial coordinate
$Nu_{x,fd}$	fully developed value of Nu_x	x_r	reattachment distance
$\overline{Nu}_x$	average Nusselt number [Eq. (43)]	Y	dimensionless transverse coordinate $(=y/z)$
n	normal to surface		
Pr	Prandtl number	Y_{mn}	difference between Y_m and Y_n
Q	surface-integrated heat transfer rate	y	transverse coordinate
q	local heat flux	z	height of enlargement step
Re_z	Reynolds number $(=\bar{u}_{in}z/\nu)$	θ	dimensionless temperature
T	temperature		$[=(T - T_{in})/(T_w - T_{in})]$
T_b	local bulk temperature	ν	kinematic viscosity
T_{in}	inlet fluid temperature	ξ	shifted Y coordinate [Eq. (8)]
T_w	temperature of lower wall of enlarged channel	Ψ	dimensionless stream function $(=\psi/\bar{u}_{in}z)$
U	dimensionless axial velocity $(=u/\bar{u}_{in})$	ψ	stream function
u	axial velocity	Ω	dimensionless vorticity
$\bar{u}_{in}$	mean velocity in pre-enlargement channel		$[=\omega/(\bar{u}_{in}/z)]$
		ω	vorticity

temperature different from that of the entering fluid flow. Both the face of the step and the upper wall of the channel are adiabatic.

The velocity problem was formulated in terms of the stream function and vorticity variables. The discretization of the conservation equations was accomplished by a control volume approach similar in spirit to that used by Patankar [1] for the primitive-variable form of the conservation equations. In the discretization of the convection terms, the conservative (or second) upwind difference was employed. For certain boundary conditions, the difference form was obtained with the aid of Taylor series. The numerical solution of the difference equations was carried out using the alternating difference implicit (ADI) technique with underrelaxation.

The energy equation was also discretized by using the control volume approach, and the ADI technique was used for the solution. The velocity and thermal solutions were performed successively for each parametrically defined case.

Owing to the aforementioned precursive effect, it was deemed inappropriate to place the upstream boundary of the solution domain at the enlargement cross section. Rather, the boundary was placed at a cross section situated at a distance h_{in} upstream of the enlargement, as indicated by the dashed line in Fig. 1.

The geometrical parameters are the channel heights h_{in} and h and the step height z $(=h - h_{in})$. The latter will be used as the characteristic length in both the Nusselt and Reynolds numbers and also to nondimensionalize the channel heights, yielding heights of $h/z = H$ and $(H - 1)$ for the post-enlargement and pre-enlargement channels. Both the dimensional and dimensionless channel and step heights are displayed in Fig. 1, as are the coordinates x, y and their dimensionless counterparts X, Y. The enlargement ratio of the channel is given by $H/(H - 1)$. The numerical results will
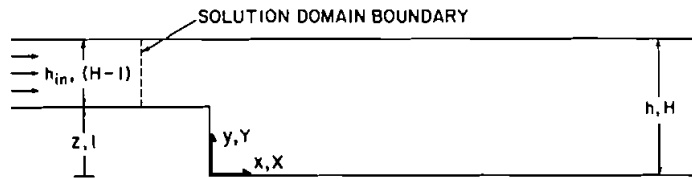
Fig. 1   Schematic diagram of the physical problem.

be parameterized by $H = 2, 3$, and 4, which correspond to enlargement ratios of 2, 3/2, and 4/3, respectively.

Another parameter of the problem is the Reynolds number Re_z based on the step height and on the mean velocity in the pre-enlargement channel. Note that the conventional hydraulic-diameter Reynolds number Re_D, which is unchanged across the enlargement, is equal to $2(H - 1)Re_z$. The parametric values of Re_z yielded Re_D values in the range from 200 to 1200. The investigated flows were, therefore, laminar.

For the solutions of the heat transfer problem, it is necessary to specify the Prandtl number. The solutions and results presented here are for a Prandtl number of 0.7, which corresponds to heat transfer in air and other gases. In [2], there are results for a Schmidt number of 0.6—the Schmidt number being the mass transfer analogue of the Prandtl number. The Schmidt number value of 0.6 corresponds to mass transfer in mixtures of water vapor and air.

For the velocity problem, the presentation of results will include reattachment distances for the separated flow spawned by the enlargement step and fluid flow patterns in the form of streamline maps. The heat transfer results will encompass isotherm maps and distributions of the local and average Nusselt numbers along the thermally active wall of the enlarged channel.

With regard to the literature, there do not appear to be prior heat transfer results for the situation investigated here. For the velocity problem, there are actually two literatures, one made up of conventional individual investigations [3–6] and the other a group study [7]. These literatures will be discussed separately.

Numerical solutions for the velocity problem were reported for the $H = 3$ case in [3–6], where [3] and [4] are companion papers. For the solutions, either of two velocity profile conditions were used at the upstream boundary of the solution domain. One of the velocity profiles was the fully developed parabolic distribution. The other velocity condition was to use experimentally determined profiles from [3] as input. The latter profiles were asymmetric and not fully developed, as will be elaborated later.

The group study [7] was organized with the objective of comparing the solutions provided by a large number of different numerical schemes, both among themselves and with experiment. Certain compulsory cases had to be solved: $H = 2$ and 3, and $Re_z = 33.3$ and 100. In addition, there were two optional cases: $H = 2$ and 3, and $Re_z = 333.3$. The size of the solution domain was prescribed, with allowance being made for the aforementioned precursive effect. The group study also included experiments for $H = 2$, $Re_z = 100$ and for $H = 3$, $Re_z = 33.3$ and 100. The pre-enlargement channel was purported to be long enough to enable hydrodynamic de-

velopment of the flow, but specific information is not given about the length of that portion of the channel.

Comparisons between the present velocity results and literature information will be made later.

GOVERNING EQUATIONS

Velocity Problem

The analysis will be performed using dimensionless variables and parameters, which include

$$X = \frac{x}{z} \qquad Y = \frac{y}{z} \qquad H = \frac{h}{z} \tag{1}$$

$$U = \frac{u}{\bar{u}_{in}} \qquad V = \frac{v}{\bar{u}_{in}} \tag{2}$$

$$\Psi = \frac{\psi}{\bar{u}_{in} z} \qquad \Omega = \frac{\omega}{\bar{u}_{in}/z} \tag{3}$$

$$Re_z = \frac{\bar{u}_{in} z}{\nu} \tag{4}$$

The velocity problem is governed by the equations for conservation of mass, x-momentum, and y-momentum. For two-dimensional flows, these equations may be recast in the vorticity, stream function form

$$\frac{\partial}{\partial X}(U\Omega) + \frac{\partial}{\partial Y}(V\Omega) = \frac{1}{Re_z}\left(\frac{\partial^2\Omega}{\partial X^2} + \frac{\partial^2\Omega}{\partial Y^2}\right) \tag{5}$$

$$\frac{\partial^2\Psi}{\partial X^2} + \frac{\partial^2\Psi}{\partial Y^2} = -\Omega \tag{6}$$

Note that the left-hand side of Eq. (5) is equivalent to $U(\partial\Omega/\partial X) + V(\partial\Omega/\partial Y)$, which is the conventional textbook representation. The present format for the left-hand side was chosen to yield the conservative form of the difference equations.

The boundary conditions for Ψ will now be considered. The value of Ψ is uniform along both the lower and upper boundaries of the channel, with a different constant value for each. Since the difference between the two constant Ψ values is the dimensionless volume flow $(H - 1)$, and since the level of Ψ is arbitrary, then

$$\Psi(\text{lower}) = 0 \qquad \Psi(\text{upper}) = (H - 1) \tag{7}$$

As already noted, the upstream boundary of the solution domain was placed at $x = -h_{in}$ or at $X = -(H - 1)$. At that station, the velocity profile is assumed to be that of a fully developed laminar flow, i.e., a parabola. Since $\Psi = \int U \, dY$ between lower and upper limits of $Y = 1$ and $Y = Y$, the Ψ distribution at the inlet of the solution domain is

$$\Psi(\text{inlet}) = (H - 1)\xi^2(3 - 2\xi) \qquad \xi = \frac{Y - 1}{H - 1} \tag{8}$$

The downstream boundary of the solution domain was placed in a region where streamwise variations are gradual. This placement was selected as an alternative to imposing the fully developed parabolic distribution at a far downstream location—too far downstream to be able to be accommodated by the available computational resources. The condition $\partial\Psi/\partial X = 0$ (i.e., $V = 0$) is too rigid to be applied upstream of the fully developed region. A more appropriate condition is

$$\frac{\partial^2\Psi}{\partial X^2} = 0 \tag{9}$$

Attention is next turned to the boundary conditions for Ω. Since Ψ is constant on all the bounding walls of the channel, it follows from Eq. (6) that

$$\Omega = \frac{-\partial^2\Psi}{\partial n^2} \qquad (n = \text{normal}) \tag{10}$$

on all the walls. At the inlet boundary, differentiation of the parabolic profile (i.e., $\Omega = -\partial U/\partial Y$) yields,

$$\Omega = -\frac{6}{H - 1}(1 - 2\xi) \tag{11}$$

At the outflow boundary, the closure condition

$$\frac{\partial\Omega}{\partial X} = 0 \tag{12}$$

is employed.

Heat Transfer Problem

For the heat transfer problem, a dimensionless temperature θ is defined as

$$\theta = \frac{T - T_{in}}{T_w - T_{in}} \tag{13}$$

where T_{in} is the temperature of the fluid entering the solution domain at $X = -(H - 1)$, and T_w is the uniform temperature of the lower wall of the enlarged channel downstream of the step. In dimensionless terms, the conservation of energy equation may be written as

$$\frac{\partial}{\partial X}(U\theta) + \frac{\partial}{\partial Y}(V\theta) = \frac{1}{Re_z Pr}\left(\frac{\partial^2\theta}{\partial X^2} + \frac{\partial^2\theta}{\partial Y^2}\right) \tag{14}$$

where Pr is the Prandtl number. The left-hand side of the equation, which is not in the standard textbook form, yields the conservative form of the difference equations.
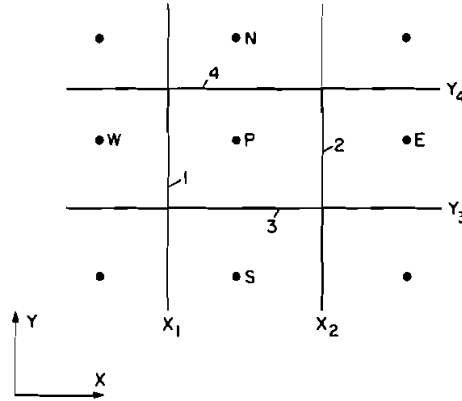
Fig. 2 Typical cluster of grid points.

On the lower wall of the enlarged channel,

$$\theta = 1 \tag{15}$$

while on all the other walls which bound the solution domain,

$$\frac{\partial\theta}{\partial n} = 0 \tag{16}$$

which expresses the adiabatic condition. At the inflow and outflow boundaries of the solution domain

$$\theta = 0 \qquad \text{and} \qquad \frac{\partial\theta}{\partial X} = 0 \tag{17}$$

DIFFERENCE EQUATIONS

The method used to discretize the governing equations will be described in terms of the vorticity equation. The energy equation is similar in form to the vorticity equation, and its discretization follows along similar lines. Furthermore, the stream function equation is simpler than the others, and it is readily discretized using the approach outlined for the vorticity equation.

A typical cluster of grid points is depicted in Fig. 2. The central grid point P in the cluster is contained within a control volume constructed so that the boundaries of the volume lie midway between the respective points. For convenience, the sides of the control volume are labeled 1, 2, 3, and 4, with corresponding coordinates X_1, X_2, Y_3, and Y_4.

To initiate the discretization, multiply Eq. (5) by $dX\,dY$ and integrate in X from X_1 to X_2 and in Y from Y_3 to Y_4. This operation yields

$$[(U\Omega)_2 - (U\Omega)_1]Y_{43} + [(V\Omega)_4 - (V\Omega)_3]X_{21} = \frac{1}{\text{Re}_z}\left\{\left[\left(\frac{\partial\Omega}{\partial X}\right)_2 - \left(\frac{\partial\Omega}{\partial X}\right)_1\right]Y_{43}\right.$$
$$\left. + \left[\left(\frac{\partial\Omega}{\partial Y}\right)_4 - \left(\frac{\partial\Omega}{\partial Y}\right)_3\right]X_{21}\right\} \tag{18}$$

where

$$X_{mn} = X_m - X_n \qquad Y_{mn} = Y_m - Y_n \tag{19}$$

Under the assumption that Ω varies linearly between adjacent grid points, the derivatives appearing on the right-hand side of Eq. (18) may be written in difference form as

$$\left(\frac{\partial\Omega}{\partial X}\right)_1 = \frac{\Omega_P - \Omega_W}{X_{PW}}, \ldots, \left(\frac{\partial\Omega}{\partial Y}\right)_4 = \frac{\Omega_N - \Omega_P}{Y_{NP}} \tag{20}$$

Inspection of the left-hand side of Eq. (18) (i.e., the convection terms) indicates that values of the velocity and vorticity on the control volume faces are needed. The evaluation of these quantities as averages of corresponding quantities at adjacent grid points can lead to numerical instability. To avoid such instability, an upwind treatment of the convection terms, termed the conservative upwind difference or second upwind difference, will be used. Thus, for example, for the $(U\Omega)_1$ term, $\Omega_1 = \Omega_W$ if $U_1 > 0$ and $\Omega_1 = \Omega_P$ if $U_1 < 0$.

To implement the foregoing description of the upwind concept at each face of all control volumes would require a large number of conditional tests and branching statements. A more efficient representation is afforded by the following expression:

$$(U\Omega)_1 = \frac{\Omega_W(U_1 + |U_1|)}{2} + \frac{\Omega_P(U_1 - |U_1|)}{2} \tag{21}$$

and similarly for the other groups on the left-hand side of Eq. (18).

With instability now avoided by the upwind treatment, the velocities at the control volume faces are obtained by averaging those at adjacent grid points, e.g.,

$$U_1 = \frac{U_P + U_W}{2} \tag{22}$$

where

$$U_P = \frac{\Psi_N - \Psi_S}{Y_{NS}} = \frac{\Psi_N - \Psi_S}{2Y_{43}} \tag{23}$$

$$U_W = \frac{\Psi_{NW} - \Psi_{SW}}{2Y_{43}} \tag{24}$$

When the various ingredients of Eq. (18) are brought together, there results

$$\alpha_N\Omega_N + \alpha_S\Omega_S + \alpha_E\Omega_E + \alpha_W\Omega_W = \alpha_P\Omega_P \tag{25}$$

in which the α's contain the unknowns Ψ_N, Ψ_S, Ψ_E, Ψ_W, Ψ_{NE}, Ψ_{SE}, Ψ_{SW}, and Ψ_{NW}, as well as geometrical parameters and Re_z. The full representation of Eq. (25) is given in Table 6.1 of [2].

An analysis such as the foregoing, when applied to the stream function equation (6), yields

$$a_N \Psi_N + a_S \Psi_S + a_E \Psi_E + a_W \Psi_W + a_P \Psi_P = \Omega_P \tag{26}$$

Here, the a's contain only geometrical parameters and are, therefore, known constants for the numerical solutions. For the energy equation, Eq. (14), the discretized form is

$$\alpha_N' \theta_N + \alpha_S' \theta_S + \alpha_E' \theta_E + \alpha_W' \theta_W = \alpha_P' \theta_P \tag{27}$$

in which the α' coefficients are identical to the α coefficients of Eq. (25), except that Re_z which appears in the latter is replaced by $\mathrm{Re}_z \mathrm{Pr}$ in the former.

Attention is now turned to the application of the boundary conditions to the finite-difference formulation of the problem. The Ψ values on the channel walls [Eq. (7)] and at the upstream boundary [Eq. (8)] are imposed at the grid points positioned on those surfaces. The Ψ condition at the downstream boundary [Eq. (9)] is implemented by writing individual Taylor series for Ψ at grid points once and twice removed from the boundary (at fixed Y). Let 0, 1, and 2 respectively denote the boundary point, the once-removed point, and the twice-removed point. Then,

$$\Psi_1 = \Psi_0 - \left(\frac{\partial \Psi}{\partial X}\right)_0 X_{01} + \left(\frac{\partial^2 \Psi}{\partial X^2}\right)_0 \frac{X_{01}^2}{2} \tag{28}$$

$$\Psi_2 = \Psi_0 - \left(\frac{\partial \Psi}{\partial X}\right)_0 (X_{01} + X_{12}) + \left(\frac{\partial^2 \Psi}{\partial X^2}\right)_0 \frac{(X_{01} + X_{12})^2}{2} \tag{29}$$

Upon setting $(\partial^2 \Psi / \partial X^2)_0 = 0$ in accordance with Eq. (9), there follows

$$\Psi_0 = \Psi_1 + (\Psi_1 - \Psi_2)\left(\frac{X_{01}}{X_{12}}\right) \tag{30}$$

which is the boundary condition employed in the numerical solutions.

With regard to the conditions on Ω, the values given by Eq. (11) are imposed at the grid points situated on the upstream boundary, while the downstream boundary condition, Eq. (12), is expressed as

$$\Omega_0 = \Omega_1 \tag{31}$$

where 0 and 1 are as in the preceding paragraph. The vorticity condition (10) at the channel walls is discretized by writing a Taylor series in Ψ at a wall-adjacent grid point wa situated at a perpendicular distance Δn from a wall grid point w. Since $(\partial \Psi / \partial n)_w = 0$ to satisfy the no-slip condition, $(\partial^2 \Psi / \partial n^2)_w = 2(\Psi_{wa} - \Psi_w)/(\Delta n)^2$. It then follows from Eq. (10) that

$$\Omega_w = -\frac{2(\Psi_{wa} - \Psi_w)}{(\Delta n)^2} \tag{32}$$

For the dimensionless temperature θ, the given values conveyed by Eq. (15) and the first of Eqs. (17) are respectively imposed at the grid points on the lower wall of the enlarged channel and on the upstream boundary of the solution domain. At all the other walls of the channel

$$\theta_w = \theta_{wa} \tag{33}$$

while at the downstream boundary of the solution domain

$$\theta_0 = \theta_1 \tag{34}$$

Two supplementary conditions are specified for the flow field in the neighborhood of the corner of the enlargement step. It was observed experimentally in [3] that the separation streamline at the corner is oriented in the X direction. This condition was incorporated into the solution by setting $\Psi = 0$ at the corner-adjacent grid point (Y = constant). Also, to avoid the ambiguity in the corner value of Ω resulting from the strict application of Eq. (32), Ω was set equal to zero there since the vorticity is zero at the detachment point of a separating streamline.

The just-derived difference equations are to be solved subject to given values of the Reynolds number Re_z and the geometrical parameter H.

COMPUTATIONAL ASPECTS

A finite-difference grid encompassing 77 points in the X direction and 77 points in the Y direction was used for the computations. The grid points were packed more tightly in the vicinity of the solid boundaries and adjacent to the corner of the step. The details of the grid point distribution are available in Appendix E of [2]. For convenience, the solution domain included the region $0 \leq Y \leq 1$, $-(H - 1) \leq X \leq 0$ upstream of the enlargement step (the solution domain is, thereby, a rectangle). However, the values of Ω, Ψ, and θ in the extended domain were held fixed during the computations and did not affect the solution in the channel proper.

If i denotes the grid point index in the X direction ($1 \leq i \leq 77$), then $i = 10$ at the step for all cases. Similarly, if j is the Y direction index ($1 \leq j \leq 77$), then $j = 55$, 47, and 39 at the step, respectively for $H = 2$, 3, and 4. The downstream boundary of the solution domain ($i = 77$) was positioned at $X = 18$, 37, and 55 for the respective H values of 2, 3, and 4.

The difference equations for Ω and Ψ are coupled and have to be solved simultaneously. The solution was obtained iteratively. First, Ψ was held fixed and the difference equations for Ω were solved. Then, this solution for Ω was used as a fixed input to the Ψ difference equations. The resulting solution for Ψ was, in turn, used as input to the Ω equations, whose solution was inputted to the Ψ equations, and so forth until convergence. The converged solution for Ψ was then used as input for the solution of the θ problem.

The foregoing procedure required a set of starting values. If a solution corresponding to the lowest Re_z for a given value of H was available, it was used to start the computations for the next Re_z for that H, and so on for successively increasing values of Re_z. For the smallest Re_z at each H, a special starting procedure, outlined

in detail in [2], had to be used for the Ω, Ψ equations. The solution for the θ problem for the smallest Re_z was started by setting $\theta = 0$.

Underrelaxation was necessary to achieve a solution for the Ω, Ψ system. In general, about 2500 iterations were required for convergence. It was not necessary to underrelax the θ problem, and convergence was always achieved within 200 iterations. About 36 hours were required to solve a given case (i.e., given H and Re_z) on an IBM PC.

The fundamental computational task was to solve a set of linear algebraic equations, either for Ω, Ψ, or θ. The combination of the large system of equations (77 × 77) and the wide bandwidth of the coefficient matrix prevents a direct solution method (e.g., Gauss elimination) from being used. Not only would the computer memory requirements be enormous, but the buildup of round-off errors associated with such a large system of equations would undermine the accuracy of the solution.

Consideration was also given to methods based on point iteration such as the Jacobi, Gauss-Seidel, and successive over-relaxation methods. These methods use the least amount of memory and are straightforward in their implementation but are slow for large systems of equations.

The alternating-direction implicit (ADI) method is believed to be the best approach for the present problem. To use the ADI method, each set of difference equations is rearranged to yield two sets of difference equations, one of which contains unknowns distributed along the X direction and the other of which contains unknowns distributed along the Y direction. Thus, for example, for Ψ, the X- and Y-direction difference equations follow from Eq. (26) as

$$a_E \Psi_E + a_W \Psi_W + a_P \Psi_P = \chi_P \tag{35}$$

$$a_N \Psi_N + a_S \Psi_S + a_P \Psi_P = \Lambda_P \tag{36}$$

Each of these equations gives rise to a banded, tridiagonal system of equations. The solution is readily obtained by making use of the tridiagonal matrix algorithm (Thomas algorithm). In using the ADI method, solutions were first obtained for the X-direction equations, after which the Y-direction equations were solved.

The computer program that was developed to solve the problem is presented in Appendix F of [2]. A detailed description of the sequence of steps executed by the program is also included in [2] along with a flow chart.

RESULTS AND DISCUSSION

Reattachment Lengths

The fluid which passes into the enlarged portion of the channel is unable to follow the abrupt offset of the lower wall of the channel. As a consequence, the flow separates from the wall, creating a pocket of recirculating fluid (i.e., a recirculation bubble) downstream of the enlargement step. The recirculation bubble is cordoned off from the mainflow by the separation streamline. The point at which the separation streamline intersects the lower wall of the enlarged channel is commonly referred to as the point of reattachment. The distance downstream of the step at which the reattachment point is situated will be called the reattachment distance

Fig. 3 Separation streamlines for
$H = 2$.
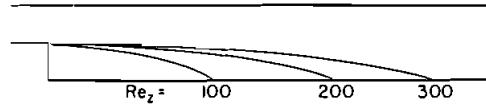
x_r. Subsequent to reattachment, the mainflow redevelops and ultimately becomes hydrodynamically fully developed.

The upcoming presentation of reattachment distances is more a prelude to comparisons with the literature than it is a reporting of altogether new results. To begin the presentation, the separation streamlines for all of the cases investigated here are displayed in Figs. 3–5. Each of the successive figures corresponds to a given enlargement, respectively characterized by $H = 2$, 3, and 4. In each figure, the separation streamline is shown for each Reynolds number Re_z used to parameterize the solutions. [Note that the conventional hydraulic diameter Reynolds number Re_D is equal to $2(H - 1)Re_z$.] To facilitate figure-to-figure comparisons, the step height z has been made the same in all three figures, which results in different channel heights.

From the figures, it is seen that for each fixed geometry, the reattachment distance increases monotonically with the step Reynolds number. The dependence of x_r on Re_z is seen to be less than linear, e.g., x_r for $Re_z = 200$ is less than twice the x_r value for $Re_z = 100$. Also, for a fixed Re_z, there is an increase of x_r/z with H. The increase is substantially greater between $H = 2$ and 3 than between $H = 3$ and 4. For the range of parameters investigated here, x_r/z ranges between 2 and 10.

A correlation of the x_r results yielded the following algebraic representation:

$$\frac{x_r}{z} = \left(0.249 - \frac{0.0626H}{H - 1}\right)Re_z^{0.777} \tag{37}$$

which deviates from the individual x_r values by no more than 1%. Equation (37) may be regarded as a formula for interpolating among the individual x_r. According to the equation, x_r/z exhibits a power-law dependence on Re_z, with the exponent being less than unity. The H dependence of x_r is manifested as a dependence on the enlargement ratio $H/(H - 1)$. As the enlargement ratio decreases (i.e., increasing H), x_r/z increases. Furthermore, as the enlargement ratio approaches unity (i.e., no enlargement), x_r/z approaches a finite value according to Eq. (37), while the step height z approaches zero and, consequently, so does x_r.

Note that the separation streamline displays a small wrinkle just downstream of the enlargement step, with the wrinkle being more in evidence as H increases. This wrinkle is believed to be extraneous, even though it also appeared in the numerical solutions of [4]. The experimental results of [3] did not show such a wrinkle.

The present results for the reattachment distance will now be compared with
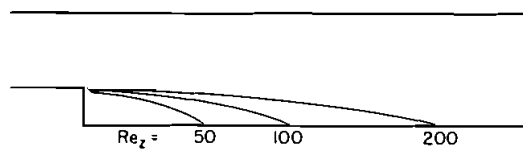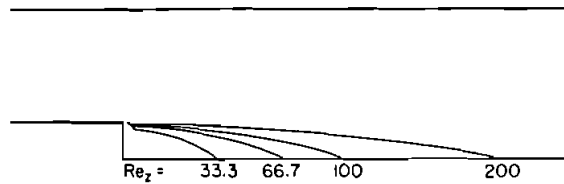

Fig. 4 Separation streamlines for $H = 3$.

Fig. 5 Separation streamlines for $H = 4$.

literature information. As noted in the Introduction, there are actually two literatures, and separate comparisons will be made with each literature, successively with the individual investigations [3–6] and then with the group study [7].

The numerical work of [3–6] was confined to the $H = 3$ case in response to the availability of the experimental results of [3] for that case. The experiments themselves were not without flaws. In particular, the pre-enlargement channel was too short for hydrodynamic development and, furthermore, the initial part of the pre-enlargement channel was asymmetric and converging.

The comparison of the $H = 3$ reattachment distances with [3–6] is made in Fig. 6, where x_r/z is plotted as a function of Re_z. Numerical predictions of x_r/z based on the assumption of a parabolic velocity distribution at the upstream boundary of the solution domain are indicated by lines representing the present investigation and Refs. [4–6]. Also plotted in Fig. 6 (open data symbols) are the numerical predictions based on the use of the experimentally determined, enlargement-section velocity profiles of [3]. The experimental data of [3] for x_r are shown as black circles.

Inspection of Fig. 6 indicates that the x_r predictions based on the experimentally determined inlet velocity profiles are, on the whole, in better agreement with the x_r data than are the predictions based on the parabolic velocity profile. A noteworthy exception to this generalization are the present numerical predictions, which agree
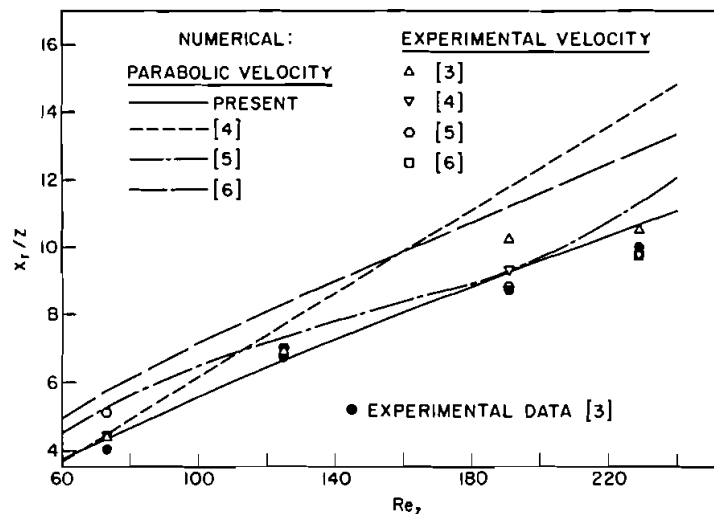

Fig. 6 Comparison of present reattachment distances with those of [3–6].

Table 1 Comparison of Present x_r/z Results with Those of [7]

H	Re_z	Exp. [7]	Present	Num. [7]
2	100	4.5	4.43	3.7–5.8
3	100	6.0	5.55	4.7–7.3

with the data almost as well as those based on the experimental profiles. This outcome lends support to the present numerical technique and testifies to the capability of a PC as a tool for solving complex fluid flows.

In passing, mention may be made of an unresolved mystery having to do with the x_r predictions of [3] and [4] based on the experimental velocity profiles. These references are companion papers, and there is no apparent reason why they should provide different x_r values based on the same model. An attempt was made to resolve this issue by private correspondence, but no response was received.

Of the four compulsory cases specified for the group study of [7], two fall within the range investigated here. The x_r results for the two cases are presented in Table 1. The table shows the x_r values from the experiments of [7], the present x_r values from Eq. (37), and the range of x_r from the various numerical schemes reported in [7]. As was true in the comparison in Fig. 6, Table 1 reveals very good agreement between the present numerical results and the experimental data, thereby adding further support to the computational tools used here. The table also shows that the various schemes reported in [7] yielded a relatively broad band of x_r values, the extremes of which were substantially in error with respect to the experimental data.

Streamline and Isotherm Maps

Representative flow field and temperature field results will be presented in terms of streamline and isotherm maps, and Figs. 7–9 have been prepared for this purpose. These figures correspond to the $H = 3$ case (intermediate among the investigated H), but the results are typical of the other cases. The successive figures, 7–9, respectively pertain to $Re_z = 50, 100$, and 200. Each figure consists of two diagrams. The upper diagram displays the streamlines, while the lower diagram displays the isotherms.

For the streamline maps, the lower boundary of the channel corresponds to $\Psi = 0$, and the upper boundary corresponds to $\Psi = (H - 1) = 2$. Away from the recirculation bubble, the successive streamlines, starting at the lower wall and proceeding upward, correspond to $\Psi = 0, 0.2, 0.4, 0.6, \ldots, 2$. Within the recirculation bubble, the increment in the stream function value between successive streamlines is -0.01. For the isotherm map, $\theta = 1$ at the lower wall, whereas the other walls are adiabatic and may experience variable θ. Starting at the lower wall and proceeding upward, the isotherms correspond to $\theta = 1, 0.9, 0.8, \ldots$.

From the streamline maps, it is seen that the mainflow glides smoothly into the enlarged portion of the channel, slipping over the fillet-like recirculation bubble with minimal perturbation. Furthermore, the mainflow appears to recover its sym-
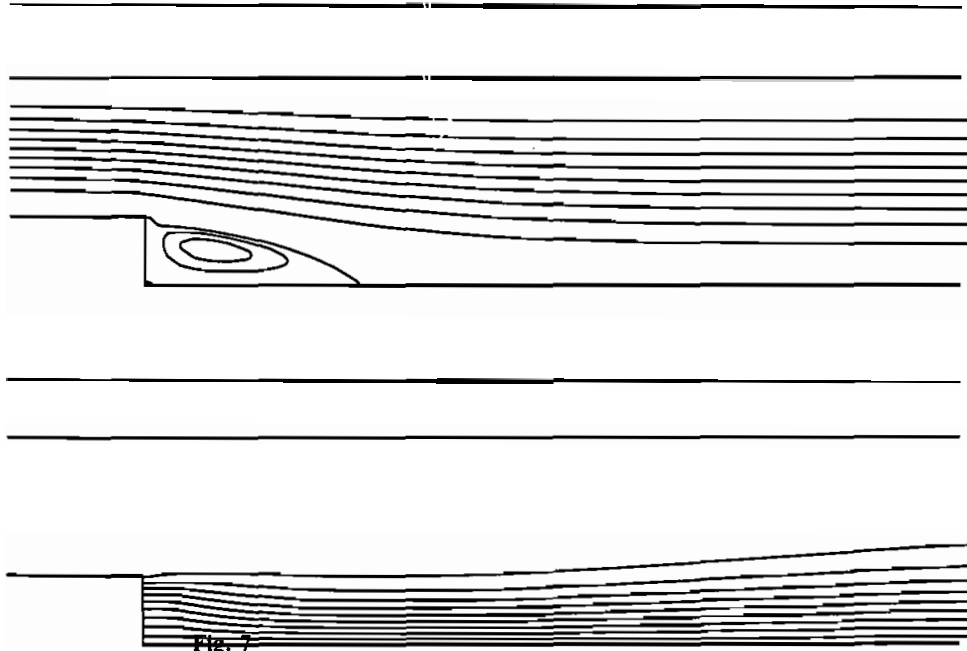
Fig. 7   Streamline and isotherm maps for $Re_z = 50$ and $H = 3$
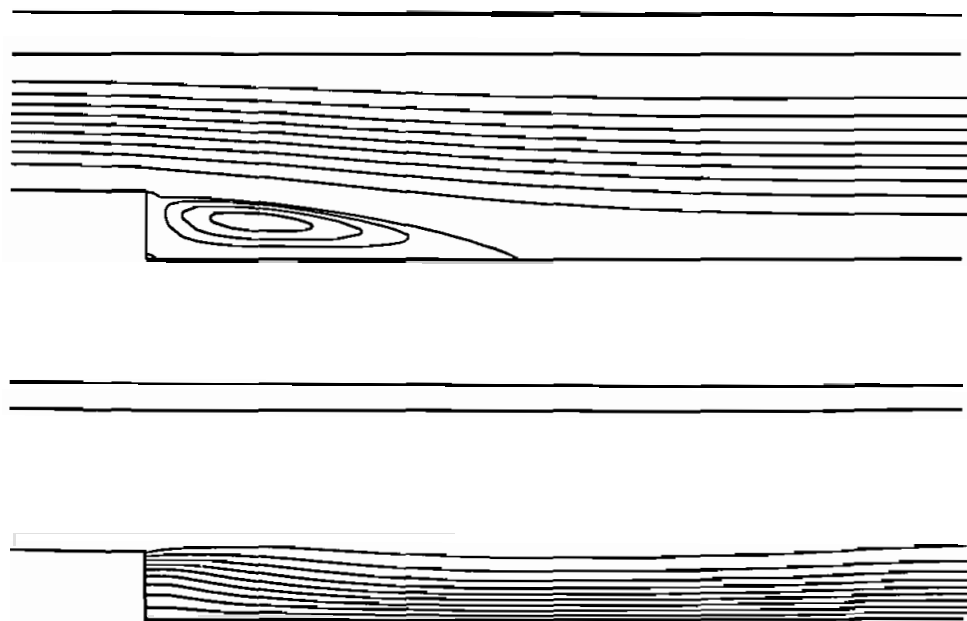
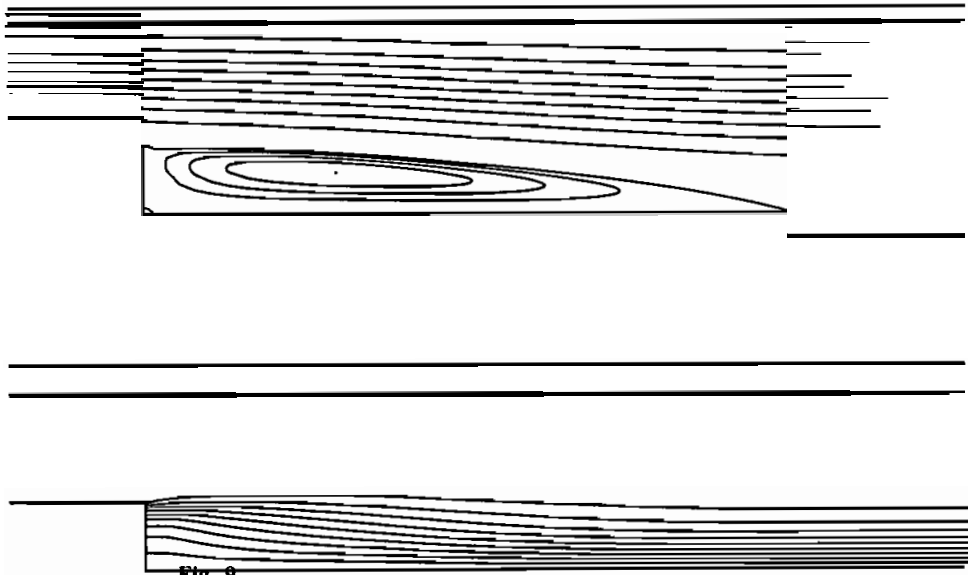**Fig. 8**   Streamline and isotherm maps for $Re_z = 100$ and $H = 3$

Fig. 9
Streamline and isotherm maps for Re$_z$ = 200 and H = 3

metry and to redevelop quite rapidly after encountering the unsymmetric abrupt enlargement. The rapidity of the recovery and redevelopment depends, not unexpectedly, on the Reynolds number, with the rapidity being greater at lower Reynolds numbers. Thus, for example, for Re$_z$ = 50, virtually perfect symmetry in the streamline deployment prevails at the downstream end of the portrayed region ($\sim x/z$ = 12). On the other hand, a modest asymmetry exists for Re$_z$ = 200, as witnessed by the slightly larger space between the Ψ = 0 and 0.2 streamlines compared with the space between the Ψ = 1.8 and 2 streamlines.

As noted earlier and confirmed in Figs. 7–9, the recirculation bubble becomes more elongated as the Reynolds number increases. In addition, the attainment of larger $|\Psi|$ values within the bubble at higher Reynolds numbers indicates an increased vigor of the recirculating flow, both absolutely and relative to the mainflow velocity. Embedded within the recirculation bubble is a diminutive, secondary recirculation zone situated at the foot of the step. The velocities within the secondary zone are very small.

It is relevant to note that at the upstream end of the recirculation bubble, the recirculating fluid has an upward velocity component. Throughout the remainder of the recirculation bubble, there is a downward velocity component. These features have a clear influence on the shapes of the isotherms. In particular, there is an upwelling of the isotherms at the upstream end of the recirculation zone, after which the isotherms tend to turn downward. Subsequent to the reattachment of the mainflow, thermal boundary layer development occurs adjacent to the lower wall of the channel. As is appropriate for a developing thermal boundary layer, the isotherms migrate away from the wall. This upward migration of the isotherms is most in evidence in the diagram for the lowest Reynolds number (i.e., in Fig. 7), since the reattachment distance is the smallest for that case.

In general, in the axial extent of the channel depicted in Figs. 7–9, there is very little thermal activity in the upper portion of the cross section. This is because there is heat transfer only at the lower wall of the channel. Only at greater downstream distances will the developing thermal boundary layer make its presence felt in the upper portion of the cross section.

Local and Average Nusselt Numbers

The local Nusselt number Nu_z at any position x on the lower wall of the channel was evaluated from its definition

$$Nu_z = \left(\frac{q}{T_w - T_{bx}}\right)\left(\frac{z}{k}\right) \tag{38}$$

Here, q is the local heat flux at x, obtained by applying the finite-difference form of Fourier's law to the numerical solutions for the temperature field, and T_w is the prescribed lower wall temperature.

The local bulk temperature T_{bx} was computed by integrating the temperature distribution across the section at x in accordance with the defining equation

$$T_{bx} = \frac{\int_0^h Tu \, dy}{\int_0^h u \, dy} \tag{39}$$

or, in terms of the variables of the analysis,

$$(T_w - T_{bx}) = (T_w - T_{in})(1 - \theta_{bx}) \tag{40}$$

where

$$\theta_{bx} = \frac{\int_0^H \theta U \, dY}{(H - 1)} \tag{41}$$

Note that in carrying out the integration indicated in Eq. (41), the velocity U takes on both positive and negative numbers in the recirculation bubble.

The average Nusselt number $\overline{Nu_z}$ was evaluated for an axial length of the lower wall between $x = 0$ and $x = x$. If Q is the rate of heat transfer for this length, i.e.,

$$Q = \int_0^x q \, dx \tag{42}$$

and $A_x = x$ is the corresponding surface area, then

$$\overline{Nu_z} = \left[\frac{Q}{A_x(\text{LMTD})}\right]\left(\frac{z}{k}\right) \tag{43}$$

The quantity (LMTD) is the conventional log-mean temperature difference

$$\text{LMTD} = \frac{(T_{in} - T_{bx})}{\ln[(T_w - T_{bx})/(T_w - T_{in})]} \tag{44}$$

or

$$\text{LMTD} = -\frac{(T_w - T_{in})\theta_{bx}}{\ln(1 - \theta_{bx})} \qquad (45)$$

The axial distributions of the local and average Nusselt numbers along the lower wall of the enlarged channel are presented in Figs. 10–12. As indicated in the legend in each figure, the local results are represented by solid lines, while dashed lines are used for the average results. Each of the figures pertains to a specific channel geometry, respectively, $H = 2$, 3, and 4 in that order. In each figure, results are given for several values of the Reynolds number Re_z.

At sufficiently large downstream distances, a thermally developed regime will be attained. That regime is characterized by a hydraulic-diameter-based, fully developed Nusselt number $Nu_{D,fd}$ equal to 4.86 (one-side-heated channel with the heated wall at uniform temperature), independent of the Reynolds and Prandtl numbers. In terms of the step height z, the fully developed Nusselt number is

$$Nu_{z,fd} = \frac{4.86}{2H} \qquad (46)$$

The fully developed Nusselt number for each enlargement case (i.e., each H) is indicated at the right-hand margin of the appropriate figure as a dot-dashed line.

An overview of Figs. 10–12 reveals numerous trends that are common to all the figures. Each local Nusselt number distribution begins with a locally low value at the foot of the enlargement step (i.e., at $x = 0$). Then, the local Nusselt number increases monotonically and attains a maximum at a location near the reattachment distance x_r. The relation between the points of maximum Nusselt number and flow reattachment is dealt with elsewhere [8]. Beyond the maximum, the local Nusselt
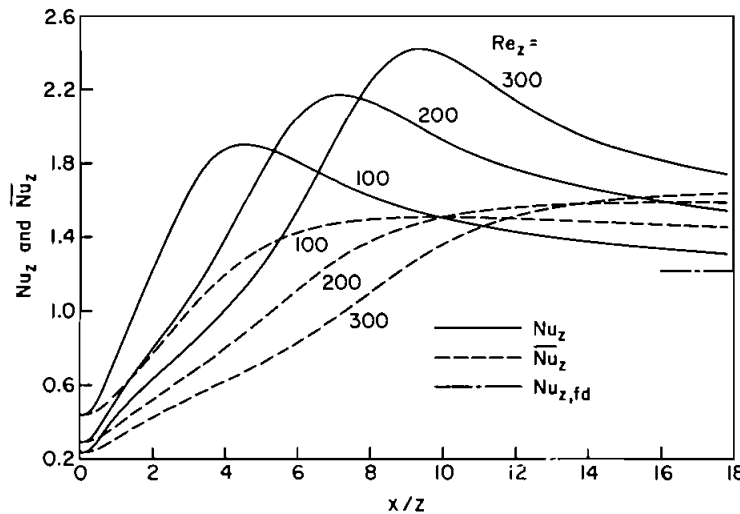

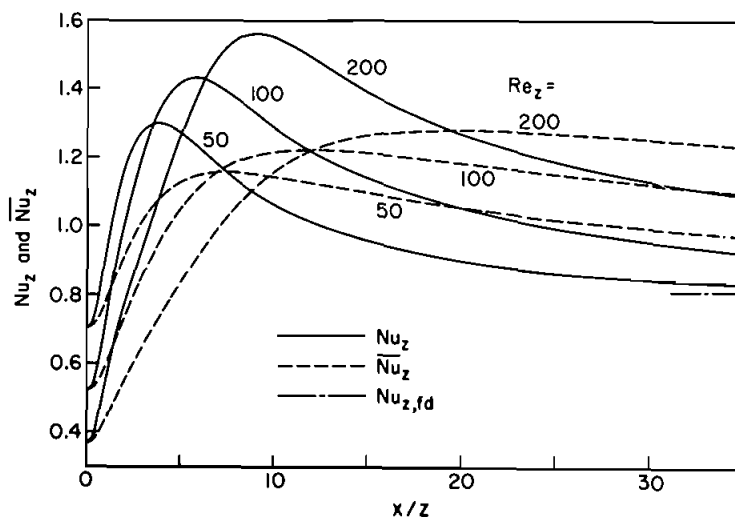Fig. 10   Local and average Nusselt number distributions for $H = 2$.

Fig. 11 Local and average Nusselt number distributions for $H = 3$.

number decreases monotonically toward the fully developed value. These characteristics of the local Nusselt number distribution reflect the separation, reattachment, and redevelopment experienced by the flow. It is noteworthy that in the absence of the enlargement and for the same heating condition, the local Nusselt number would have attained a very high value at $x = 0$ and then decreased monotonically toward the fully developed regime with increasing x.

The average Nusselt number distributions are not, strictly speaking, the averages of the corresponding local distributions, as can be seen from an examination of Eqs. (38)–(45). However, the qualitative trends displayed by the average Nusselt
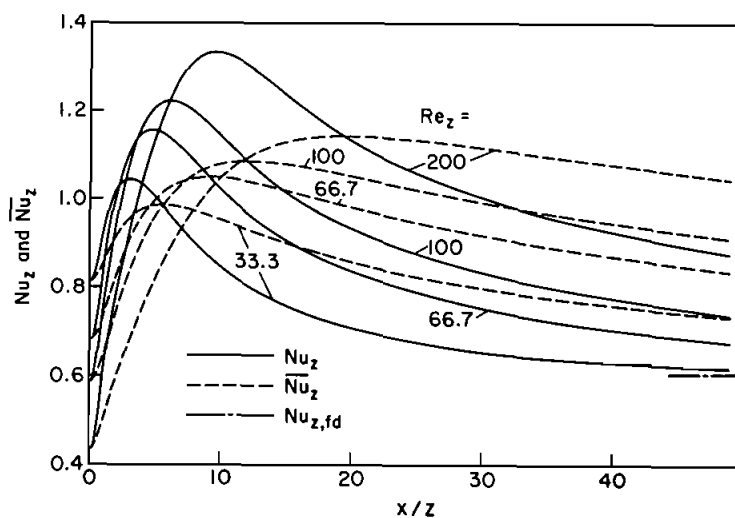

Fig. 12 Local and average Nusselt number distributions for $H = 4$.
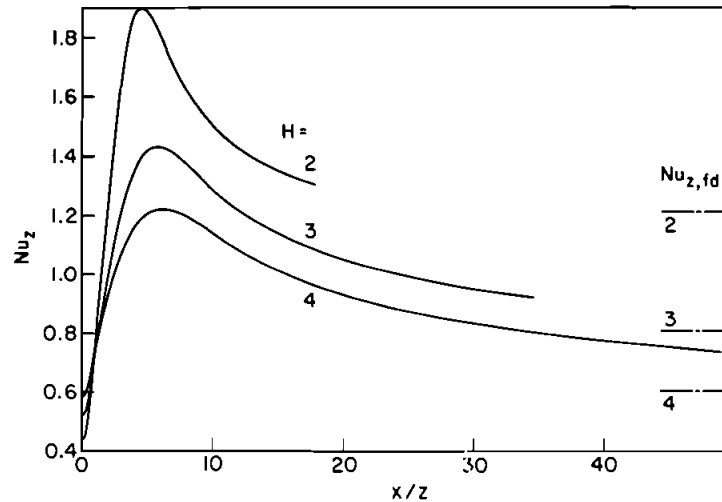
Fig. 13 Local Nusselt number distributions for $Re_z = 100$.

number distributions are the same as those of the averaged local distributions. The average Nusselt number starts with the same value as the local Nusselt number but rises more slowly. It continues to rise even when the local Nu has attained its maximum and is decreasing. Only when the ascending average Nu and the descending local Nu intersect does the former begin to drop off. The dropoff of the average Nu is substantially slower than that of the local although, with sufficient downstream distance, it, too, will attain the indicated fully developed value.

Inspection of any one of Figs. 10–12 indicates that the lower the Reynolds number, the earlier are the maxima achieved for both the local and average Nu. Furthermore, the fully developed Nusselt number is attained at shorter distances from the enlargement step at lower Reynolds numbers. This occurs because at lower Reynolds numbers, the recirculation bubble is shorter and the thermal boundary layer growth downstream of the bubble is more rapid.

The elongation of the recirculation bubble with increasing Reynolds number and the related downstream shift of the Nu maximum gives rise to a complex dependence of the Nusselt number on the Reynolds number for a fixed geometry (i.e., fixed H). From Figs. 10–12, it is seen that there is a range of x/z downstream of the step in which the Nusselt number actually decreases monotonically with increases of the Reynolds number! After that, there is a range of x/z where the Nusselt-Reynolds variation is nonmonotonic, increasing at first and then decreasing. Next is a region in which the Nusselt number increases monotonically with the Reynolds number. Finally, at sufficient downstream distances (i.e., in the fully developed regime), the Nusselt number is independent of the Reynolds number. It is worthy of note that the maximum Nusselt number increases monotonically as the Reynolds number increases.

The local Nusselt number results are presented in a new perspective in Figs. 13 and 14 and similarly for the average Nusselt number in Figs. 15 and 16. Each
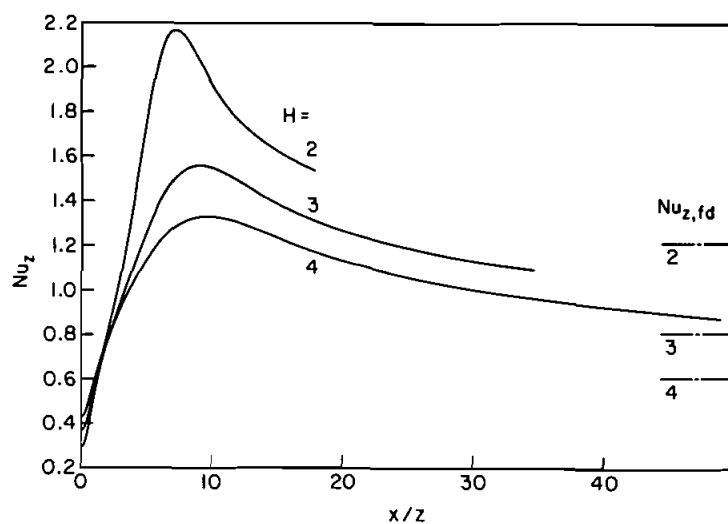
Fig. 14   Local Nusselt number distributions for $Re_z = 200$.

of these figures corresponds to a fixed value of Re_z, namely, 100 for Figs. 13 and 15, and 200 for Figs. 14 and 16. In each figure, the Nusselt number, either Nu_z or $\overline{Nu}_z$, is plotted as a function of x/z for parametric values of the enlargement parameter H. Note that in each figure, z appears in the ordinate variable, the abscissa variable, the curve parameter, and in the figure parameter. Therefore, any qualitative interpretations of the results conveyed in each figure are best made at a fixed z, so that increasing H corresponds to increasing channel heights.

Figures 13 and 14 show that except for a small region adjacent to the enlargement step, the smaller the value of H, the larger is the local Nusselt number. If the
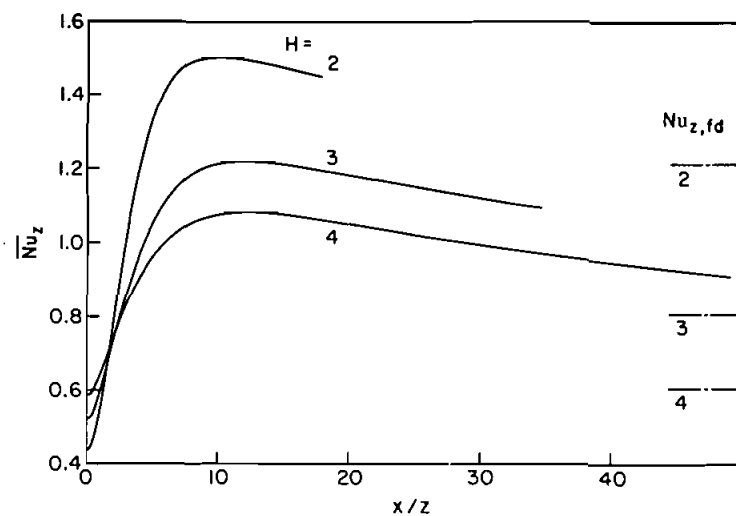

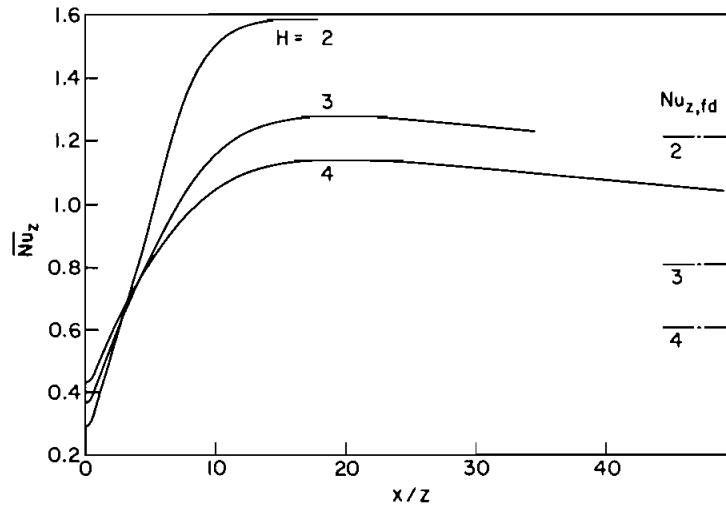Fig. 15   Average Nusselt number distributions for $Re_z = 100$.

Fig. 16   Average Nusselt number distributions for $Re_z = 200$.

step height is fixed, this means that the Nusselt number is larger for channels of lower height, a trend which is physically reasonable. An opposite ordering of the Nusselt numbers is seen to occur adjacent to the step, a result which reflects the localized response of the velocity of the recirculating flow at the upstream end of the recirculation bubble.

There is a clear downstream shift of the location of the Nusselt number maximum as H increases from 2 to 3, but the shift is less marked with an increase in H from 3 to 4. By comparing Figs. 13 and 14, it is clear that as Re_z increases, the maxima shift to the right and the approach to fully developed conditions is delayed.

The foregoing discussion of Figs. 13 and 14 is generally applicable to Figs. 15 and 16. The main difference between the sets of figures is the dampening and delaying effect of the averaging.

CONCLUDING REMARKS

The work reported here has demonstrated that a PC can be used effectively in solving complex problems of convective heat transfer and fluid flow. The accuracy of the present velocity field solutions was shown to be at least as good as that of prior numerical solutions. Furthermore, the present velocity solutions have extended the range of the investigated enlargements from $H = 2$ and 3 to $H = 2$, 3, and 4.

The heat transfer solutions obtained here are, seemingly, the first of their kind. Because of the elongation of the recirculation bubble with the Reynolds number, the variation of the local Nusselt number with the Reynolds number took on different forms at various axial distances from the enlargement step. In a region extending downstream from the step, the local Nusselt number actually decreased monotonically with increasing Reynolds number! At greater downstream distances, the Nusselt-Reynolds variation was nonmonotonic, but, beyond that, the Nusselt number increased with the Reynolds number. Finally, much farther downstream, in the ther-

mally developed regime, the Nusselt number was independent of the Reynolds number.

REFERENCES

1. S. V. Patankar, *Numerical Heat Transfer and Fluid Flow*, Hemisphere, Washington, D.C., 1980.
2. W. Chuck, Evaporation of Water from a Recessed Surface to a Parallel Forced Convection Airflow, Ph.D. Thesis, Dept. of Mechanical Engineering, University of Minnesota, Minneapolis, 1985.
3. M. K. Denham and M. A. Patrick, Laminar Flow over a Downstream Facing Step in a Two Dimensional Channel, *Trans. Inst. Chem. Eng.*, vol. 52, pp. 361–367, 1974.
4. D. J. Atkins, S. J. Maskell, and M. A. Patrick, Numerical Predictions of Separated Flows, *Int. J. Numer. Methods Eng.*, vol. 15, pp. 129–144, 1980.
5. C. E. Thomas, K. Morgan, and C. Taylor, A Finite Element Analysis of Flow Over a Backward Facing Step, *Comput. Fluids*, vol. 9, pp. 265–278, 1981.
6. L. P. Hackman, G. D. Raithby, and A. B. Strong, Numerical Prediction of Flows over Backward Facing Steps, *Int. J. Numer. Methods Fluids*, vol. 4, pp. 711–724, 1984.
7. K. Morgan, J. Periaux, and F. Thomasset (eds.), *Analysis of Laminar Flow Over a Backward Facing Step: A GAMM Workshop*, Friedr. Vieweg und Sohn, Braunschweig, Weisbaden, 1984.
8. E. M. Sparrow, S. S. Kang, and W. Chuck, Relation Between the Points of Flow Reattachment and Maximum Heat Transfer for Regions of Flow Separation, *Int. J. Heat Mass Transfer*, in press.